Wave Motion 136 (2025) 103527

Contents lists available at ScienceDirect

Wave Motion

journal homepage: www.elsevier.com/locate/wamot

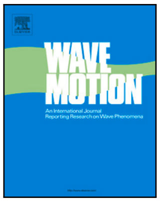

Analytical modeling of damped locally-resonant metamaterials

Sabiju Valiya Valappil [a,*], Alejandro M. Aragón [b]

[a] Faculty of Applied Sciences, Delft University of Technology, Lorentzweg 1, 2628 CJ, Delft, The Netherlands
[b] Faculty of Mechanical Engineering, Delft University of Technology, Mekelweg 2, 2628 CD Delft, The Netherlands

ARTICLE INFO

Keywords:
Phononic crystals
Locally-resonant metamaterials
Spectral element method
Finite element method
Lumped mass method
Damping
Viscoelasticity
Band structure
Transmissibility

ABSTRACT

Locally-resonant metamaterials (LRMMs) are architected materials that can be designed to manipulate mechanical wave propagation by tuning their band gaps. Discrete lumped-mass models and discrete distributed-mass finite element models are both generally used to analyze LRMMs. While the former is accurate only near the fundamental resonance frequency of resonators, the latter's accuracy is tightly coupled to the computational cost. In this study, an analytical procedure based on the spectral element method (SEM) is proposed to analyze both undamped and damped LRMMs as continuous systems. We compare LRMMs' band structures to those obtained by discrete models and show that the proposed procedure is capable of capturing the wave dynamics of these materials very accurately and with negligible computational cost. The behavior of a finite LRMM waveguide is also studied through displacement transmissibility. In addition to the attenuation provided by band gaps, we investigate the effects of constant viscous damping and frequency-dependent viscoelastic damping, which proved to be a straightforward extension of the undamped spectral element model.

1. Introduction

Phononic crystals (PnCs) are architected materials where band gaps (BGs)—*i.e.*, ranges of mechanical wave frequencies whose propagation is forbidden—are caused by the periodicity of scatterers and the impedance mismatch at material interfaces [1]. In PnCs, the BGs are therefore produced by Bragg scattering at a frequency that is determined by the size of the periodic unit cell (PUC), and therefore the operating frequencies are strongly limited by their size. Locally-resonant metamaterials (LRMMs) overcome this limitation since BGs due to Bragg scattering occur together with those produced by Mie scattering around the resonance frequency of resonators placed periodically in the material [2]. By decoupling the target band gap from the dimensions of the PUC, LRMMs can be tuned to target sub-wavelength scales, *i.e.*, band gaps with frequencies smaller than those obtained by PnCs. Because of BGs, LRMMs, and PnCs have been explored in many applications, including vibration isolation [3], acoustic diodes and transistors [4,5], energy harvesting [6], super/hyper acoustic lenses [7,8], acoustic antennas [9], frequency steering [10,11], acoustic cloaking [12–15], metasurfaces for phase manipulation [16] and high-resolution acoustic devices [17]. The design of LRMMs for practical applications requires a thorough understanding of their behavior. Since characterizing them experimentally is a tedious and expensive exercise, various analytical and numerical methods have been proposed. These can be classified in discrete lumped-mass [18], discretized distributed-mass [19], and continuous distributed-mass methods [20]. Notice that while discrete is the opposite of distributed mass, the terms discretized and continuous refer to the governing partial differential equations (PDEs).

Lumped-mass methods (LMM) have been widely used to model LRMMs. Huang et al. [18,21–24] proposed a one dimensional (1D) undamped discrete lumped-mass model in which the host and the resonator are represented as interconnected springs and

---

[*] Corresponding author.

E-mail addresses: S.ValiyaValappil@tudelft.nl (S.V. Valappil), a.m.aragon@tudelft.nl (A.M. Aragón).
URLs: https://www.tudelft.nl/en/2022/tnw/sabiju-valiya-valappil-joined-imphys-as-post-doc (S.V. Valappil), https://3me.tudelft.nl/aaragon (A.M. Aragón).

https://doi.org/10.1016/j.wavemoti.2025.103527
Received 25 October 2024; Received in revised form 8 February 2025; Accepted 15 February 2025

masses. Along with its simple implementation, this model is straightforward to extend to include more complex phenomena such as nonlinear behavior [25–28]. Hussein and Frazier [29–32] extended this LMM to incorporate the influence of damping in PnCs and LRMMs. They compared the effects of Rayleigh, viscous, and viscoelastic damping in the dispersion relation. Huang and Sun further extended LMMs and incorporated multiple resonators to capture multiple BGs [33]. 1D LRMMs using LMMs have been studied for several applications, including broadband elastic wave absorbers [34,35] and broadband wave control using nonlocal elastic metasurfaces [36], active control of band gaps [37], and blast-wave impact mitigation [38]. On the downside, considering the host and resonator as linear springs and point masses forbids LMMs from obtaining an accurate response at frequencies beyond the first BG (the first two modes). Therefore, the behavior at higher frequencies mandates distributed-mass models.

Many discretized distributed-mass methods have been proposed to analyze LRMMs. The plane wave expansion method [39–41] is a semi-analytical procedure that obtains the dynamic response by formulating an eigenvalue problem and by solving it iteratively. The method, however, has difficulties in simulating LRMMs with highly contrasting elastic properties [42]. The transfer matrix method (TMM) [43,44] analyzes LRMMs by means of transfer matrices that transform a state vector comprised of displacement and force from one unit cell to the next. The advantage of the method lies in its versatility in deriving the transfer matrices, *i.e.,* analytical, numerical, or experimental data can be used to formulate them. However, the analysis of LRMMs with TMM suffers from numerical instabilities under extreme conditions such as a large change in stiffness values between adjacent elements [45]. The boundary element method (BEM) analyzes LRMMs by transforming the PDEs to boundary integral equations and solving them over the boundary [46]. The main advantage of this method is that only the boundary needs to be discretized, resulting in system sizes smaller than those obtained by methods where the entire continuum is discretized. Yet, the implementation of BEM is not straightforward and it leads to fully dense asymmetric matrices, which are harder to solve than the sparse banded symmetric matrices that result from the finite element method (FEM) [47]. In the latter, which is also commonly used because of its versatility in discretizing complex geometries, BGs due to both Mie and Bragg scattering can be captured by representing the LRMM as a series of interconnected finite elements (FEs) [19,48,49]. Matlack et al. [50] used FEM to explore the broadband capabilities of LRMMs by combining both Bragg and Mie scattering. Optimization of the LRMMs for broad BGs was carried out in [51,52]. In addition, it is straightforward to add damping to the formulation. Pai et al. [53] and Nobrega et al. [54] used FEM to study the effects of viscous damping in LRMMs. Khajehtourian and Kochmann [55] studied the viscous damping effect of LRMMs using FEM and LMM. The effects of viscoelasticity in the band structure of PnCs and LRMMs using Kelvin–Voigt and generalized Maxwell models have also been studied [56–58]. Nevertheless, as FEM requires at least eight linear elements to represent a wave period [59] accurately, and thus the required number of degrees of freedom (DOFs) increases with frequency. As a result, analyses (both band structure and transmissibility) become extremely expensive at high frequencies. To overcome this, Shi et al. [60,61] used the time-dependent spectral element method (*t*-SEM), whereby using high-order polynomials (Gauss–Lobatto–Legendre basis functions) to define the approximation, computational efficiency is greatly improved [62,63]. For the same target frequency, *t*-SEM has a significant reduction in the number of finite elements when compared to standard FEM based on linear shape functions.

All methodologies above discretize the continuum equations that describe the dynamics of the system. There are, however, methodologies where such discretization is not needed (or at least not entirely). We deem these as continuous distributed-mass methods. The spectral element method (SEM) [64] is an analytical procedure predominantly used to solve wave propagation problems. Because the shape functions used in SEM are based on the solution to the wave equation, the response obtained by the method is exact in the frequency domain. Yet, SEM cannot deal with complex geometries in 2D and 3D for which the wave solutions are not known and it is unable to solve nonlinear problems directly [65], since the method is based on fast/discrete Fourier transform (FFT/DFT) techniques. In addition, due to FFT/DFT truncation, the method is discrete in the time domain and thus the solutions are not as accurate as in the frequency domain. Since shape functions used in SEM are frequency-dependent, changing the frequency does not affect the system size, *i.e.*, only one element is needed to resolve the wave propagation through it irrespective of frequency. Given the analytical nature of the method, increasing the number of SEM elements per section does not improve the solution, so there is no need for mesh convergence studies as usually carried out with standard finite element procedures. In addition, a special spectral element called a throw-off element [64] aids in modeling non-reflective boundary conditions effectively.

From all distributed-mass methods, SEM is the most accurate and least computationally expensive approach to analyze linear LRMMs in the frequency domain. The special properties of SEM were first explored in the context of 1D LRMMs by Xiao et al. [20], who considered a uniform rod as a host with periodically attached multi-DOF spring-mass resonators. Later, Nobrega et al. [54] verified the accuracy of SEM by comparing it to FEM and obtained a matching response. Xiao et al. [66] also studied LRMMs with beam-type resonators attached to a homogeneous beam. Casadei and Bertoldi used SEM to model the wave propagation through a beam immersed in a fluid containing a periodic array of airfoil resonators [67]. They considered the host as an SEM beam element and the resonators as point masses connected by linear springs that also include the viscous damping behavior of the resonator. In both [66,67], the resonators were treated as lumped masses. The literature on the use of SEM considering damping is scarce (in works [20,54,66] LRMMs are undamped). SEM has also been explored to analyze other periodic structures, such as the vibration analysis of three-dimensional Kagome lattices by Wu et al. [68], whose model matched corresponding FEM results. The same authors further used SEM to characterize lattice structures inspired by butterfly wing surfaces with hierarchical periodicity [69]. In a context different from periodic structures, Song et al. [70] studied the viscoelastic damping behavior of a composite beam with SEM by incorporating frequency-dependent elastic moduli to the dynamic stiffness matrix. To the best of our knowledge, there are no studies concerning the modeling of LRMMs with the presence of viscous and viscoelastic damping as continuous systems, where BGs due to the higher modes of the resonator and Bragg scattering are also present.

In this study, we model 1D LRMMs as continuous systems using SEM and compare the dispersion relation to those obtained by LMM and FEM. In addition, we characterize a finite LRMM waveguide composed of five PUCs by obtaining displacement transmissibility. To capture the effects of damping, we consider constant viscous damping and linear viscoelastic damping in our models. The former acts as a constant dissipation component depending on the system velocity, whereas in the latter, the dissipation has a term that varies with the input frequency (similarly to [70] for a composite beam). Kelvin–Voigt and generalized Maxwell models are used to include viscoelastic effects. We show the effect of damping in LRMMs by comparing displacement transmissibility between undamped and damped models.

2. Problem description

Consider an LRMM waveguide Ξ composed of n PUCs such that its closure is defined as $\overline{\Xi} = \cup_{i=1}^{n} \overline{\Pi}_i \subset \mathbb{R}$ (see Fig. 1). The ith PUC $\Pi_i \subset \Xi$ of length L is subdivided into subdomains Ω_j, $j = 1, \dots, p$ such that $\overline{\Pi} = \cup_{j=1}^{p} \overline{\Omega}_j$. The interfaces between contiguous subdomains are denoted $\Gamma_{jk} = \overline{\Omega}_j \cap \overline{\Omega}_k, j \neq k$. The jth subdomain of length l_j and cross-sectional area A_j has elastic modulus E_j, density ρ_j, and damping factor η_j. A_j, $j = 1, \dots, p$ may be different for each subdomain but is kept constant within it. In this study, we consider a PUC composed of five subdomains ($p = 5$) and the complete waveguide also composed of five PUCs ($n = 5$), as shown in Fig. 1. The LRMM is designed such that adjacent subdomains possess high contrast in stiffness and mass in order to produce wide BGs due to Bragg scattering. Moreover, material properties are chosen such that the system behaves as a host containing resonators that also produce BGs due to Mie scattering. To that end, we select teflon, rubber, and lead for Ω_1, Ω_2, and Ω_3, respectively. To retain structural symmetry, Ω_1 is made equivalent to Ω_5, and Ω_2 to Ω_4. Here, the resonator is composed of subdomains Ω_2, Ω_3, and Ω_4. The material properties are listed in Table 1.

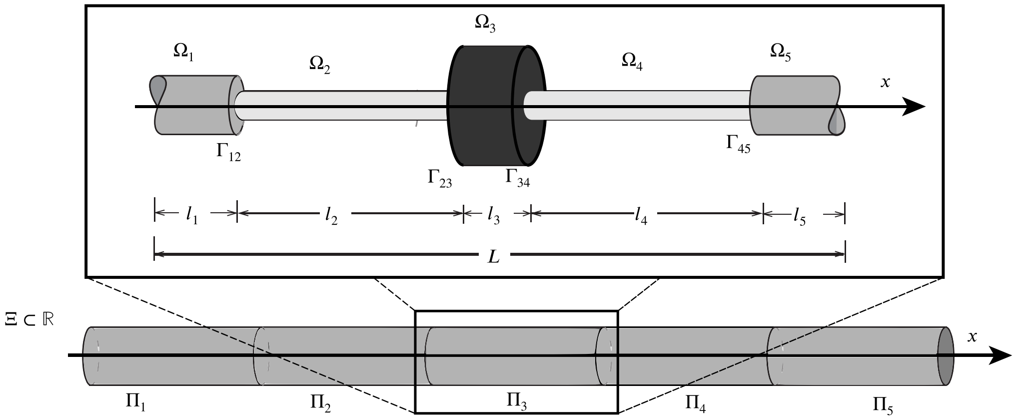

Fig. 1. Waveguide Ξ composed of five periodic unit cells Π_i. Each PUC of the LRMM is composed of five subdomains Ω_j that are connected at interfaces Γ_{jk}. L and l_j, respectively, represent the lengths of PUC and of the jth subdomain. Also, Ω_1 and Ω_5 are equivalent, and so are Ω_2 and Ω_4.

Table 1
Material properties for PUC's subdomains.

Material	Density (kg/m^3)	Young's modulus (GPa)	Damping ratio
Teflon	2200	0.45	0.13
Rubber	1105	0.0103	0.4
Lead	11340	13	0.1

The equation that describes the wave propagation in the LRMM, in the absence of body forces, is given by:

$$E_j A_j \frac{\partial^2 u_j}{\partial x^2} - \eta_j \frac{\partial u_j}{\partial t} - \rho_j A_j \frac{\partial^2 u_j}{\partial t^2} = 0 \qquad \forall\, \Omega_j \in \Xi, \tag{1}$$

where x and t represent the spatial coordinate and time, respectively, η_j is the jth subdomain's damping factor, which is obtained as the product between damping ratio (from Table 1) and the critical damping factor $c_c = 2\sqrt{m_j k_j}$, with m_j and k_j denoting the mass and stiffness of the jth subdomain, respectively. With $N = EA\partial u/\partial x$ denoting the axial load, interface conditions are given by:

$$u_j = u_k \quad \text{and} \quad N_j = N_k \qquad \forall\, \Gamma_{jk} \in \Xi. \tag{2}$$

To fully define the boundary value problem (BVP), the boundary conditions are still needed. In this paper, we study two BVPs, for which the BCs are:

1. **BVP 1: Band structure analysis** (or dispersion analysis) A dispersion relation, which establishes a relationship between frequency ω and wave vector q, is used to describe the effect of dispersion on the properties of waves in a medium. This

relation is obtained by conducting an eigenvalue analysis of the PUC after providing Bloch–Floquet periodic boundary condition (BFPBC) [71]. Since the PUC contained five bar elements, the periodicity is applied from the first (u_1) to the fifth (u_5) element.

$$u_5(L,t) = e^{\mathrm{i}qL} u_1(0,t), \tag{3}$$

where i represents the imaginary number, and $q = 1/\lambda$ the Bloch wave vector, with λ denoting the wavelength. Considering the real part of the wave vector in the dispersion relation gives us insight into BGs and wave speeds corresponding to different wave propagation modes. Considering the imaginary part of the wave vector gives us an indication of the attenuation rate for a given frequency within a BG.

2. **BVP 2: Transmissibility analysis** (or harmonic frequency sweep analysis) is the steady-state dynamic analysis of the finite LRMM waveguide Ξ after applying the essential (Dirichlet) boundary condition [72]:

$$u(0,t) = u_0 e^{\mathrm{i}\omega t}, \tag{4}$$

where u_0 is the constant displacement amplitude applied at one end of the waveguide (at $x = 0$) and ω is the applied frequency. For a given frequency, the transmissibility relation provides the reduction in amplitude of the input signal for a given number of PUCs.

The weak or variational form of Eq. (1), which can be obtained by the method of weighted residuals, is given by: Find $u_j \in \mathcal{U}$ such that

$$\sum_{j\in\mathcal{J}} \left[\int_{\Omega_j} E_j A_j \frac{\partial u_j}{\partial x} \frac{\partial w_j}{\partial x}\, \mathrm{d}x + \int_{\Omega_j} \rho_j A_j \frac{\partial^2 u_j}{\partial t^2} w_j \,\mathrm{d}x + \int_{\Omega_j} \eta_j \frac{\partial u_j}{\partial t} w_j \,\mathrm{d}x \right] = \sum_{j\in\mathcal{J}} \left[w_j N_j \right]_0^{l_j} \quad \forall\, w_j \in \mathcal{V}, \tag{5}$$

where w is the weight function, $\mathcal{U}, \mathcal{V}$ are sufficiently-smooth function sets, and $\mathcal{J}$ is the index set of subdomains analyzed and depends on the boundary value problem; for **BVP 1**, $\mathcal{J} \equiv \mathcal{J}_\Pi = \{1,\dots,5\}$ whereas for **BVP 2**, $\mathcal{J} \equiv \mathcal{J}_\Xi = \{1,\dots,25\}$. It is worth noting that, although the traction boundary condition was given for completeness of the right-hand-side of Eq. (5), its contribution eventually vanishes because tractions at an interface Γ_{jk} from contiguous subdomains Ω_j and Ω_k cancel one another, leaving only those at the ends of Π (or Ξ) for which we conveniently choose $w_j = 0$.

The infinitely dimensional weak form given by Eq. (5) is then solved with FEM, where we adopt finite element function sets $\mathcal{U}^h \subset \mathcal{U}, \mathcal{V}^h \subset \mathcal{V}$ spanned by linear shape functions. In the case of SEM, we solve the strong form Eq. (1) by means of frequency-dependent shape functions that are discrete in time due to the use of FFT/DFT. We also analyze the LRMM PUC using a lumped-mass method by applying force balance. Damping is not considered in FEM and LMM models.

2.1. SEM analysis

To obtain the solution of Eq. (1) by means of the spectral element method, we first derive the shape functions that will be used in each spectral element. In the jth subdomain, the solution to Eq. (1) is assumed in spectral form as [65]:

$$u_j(x,t) = U_j(x,\omega)\,\mathrm{e}^{\mathrm{i}\omega t} \qquad \text{in } \Omega_j, \tag{6}$$

where $U_j(x,\omega)$ is the spatial component of the displacement. Substituting Eq. (6) in Eq. (1) provides us with the equation of motion in spatial form:

$$E_j \frac{\partial^2 U_j}{\partial x^2} + \left(\omega^2 \rho_j - \mathrm{i}\omega\eta_j/A_j\right) U_j = 0 \qquad \text{in } \Omega_j. \tag{7}$$

The general solution of Eq. (7) in the jth subdomain is

$$\begin{aligned} U_j(x,\omega) &= B_{j,1}\mathrm{e}^{-\mathrm{i}\kappa_j(\omega)x} + B_{j,2}\mathrm{e}^{\mathrm{i}\kappa_j(\omega)x} \\ &= \begin{bmatrix} e^{-\mathrm{i}\kappa_j(\omega)x} & e^{\mathrm{i}\kappa_j(\omega)x} \end{bmatrix} \begin{bmatrix} B_{j,1} \\ B_{j,2} \end{bmatrix} = \boldsymbol{e}(x,\omega)\,\boldsymbol{B}_j. \end{aligned} \tag{8}$$

where $B_{j,1}$ and $B_{j,2}$ denote the amplitudes of the forward and backward traveling waves and $\kappa_j(\omega)$ the longitudinal wave vector with the effect of damping, given by:

$$\kappa_j(\omega) = \sqrt{\tilde{\kappa}_j^2 - \mathrm{i}\omega\eta_j/E_jA_j}, \tag{9}$$

with $\tilde{\kappa}_j = \omega/c_j$ is the non-dispersive longitudinal wave vector, and $c_j = \sqrt{E_j/\rho_j}$ is the longitudinal wave speed. For a finite spectral element of length l_j, the displacement field can be written as:

$$\boldsymbol{U}_j = \begin{bmatrix} \boldsymbol{e}(0,\omega) \\ \boldsymbol{e}(l_j,\omega) \end{bmatrix} \boldsymbol{B}_j = \begin{bmatrix} 1 & 1 \\ \mathrm{e}^{-\mathrm{i}\kappa_j(\omega)l_j} & \mathrm{e}^{\mathrm{i}\kappa_j(\omega)l_j} \end{bmatrix} \begin{bmatrix} B_{j,1} \\ B_{j,2} \end{bmatrix}. \tag{10}$$

Using Eq. (10), we can eliminate the amplitude vector $\boldsymbol{B}_j$ from Eq. (8) to yield the displacement in the spectral element in terms of nodal DOFs as:

$$U_j(x,\omega) = \boldsymbol{\Phi}_j(x,\omega)\,\boldsymbol{u}_j, \tag{11}$$

where $\boldsymbol{\Phi}_j = \left[\csc\left(\kappa_j l_j\right)\sin\left[\kappa_j\left(l_j - x\right)\right] \quad \csc\left(\kappa_j l_j\right)\sin\left(\kappa_j x\right)\right]$ is the vector of frequency-dependent shape functions.

Since Eq. (11) is the exact solution of Eq. (7), we can simply use force balance to derive the stiffness matrix, *i.e.*, $\boldsymbol{f}_j(\omega) = \boldsymbol{s}_j(\omega)\boldsymbol{u}_j$, where $\boldsymbol{f}_j = \left[-N_j(0) \quad N_j\left(l_j\right)\right]^{\intercal}$ denotes the self-equilibrating force vector—with components being the axial force evaluated at the end nodes—and $\boldsymbol{s}_j$ denotes the symmetric dynamic stiffness matrix (DSM) given by:

$$\boldsymbol{s}_j(\omega) = \begin{bmatrix} a_j & b_j \\ b_j & a_j \end{bmatrix}, \tag{12}$$

where:

$$\begin{aligned} a_j &= \frac{E_j A_j}{l_j}\left(\kappa_j l_j\right)\cot\left(\kappa_j l_j\right), \\ b_j &= -\frac{E_j A_j}{l_j}\left(\kappa_j l_j\right)\csc\left(\kappa_j l_j\right). \end{aligned} \tag{13}$$

Note that the shape functions and DSM for an undamped rod can be obtained by supplying $\eta = 0$, in which case $\kappa_j(\omega)$ reduces to $\tilde{\kappa}_j(\omega)$. As mentioned above, for SEM, only one element is required per subdomain Ω_j.

For a PUC, we can obtain the global dynamic stiffness matrix $\boldsymbol{S}$ by assembling the contributions of all subdomains, *i.e.*, $\boldsymbol{S} = \mathbb{A}_{j\in\mathcal{J}_\Pi}\boldsymbol{s}_j$, where $\mathbb{A}$ denotes the assembly operator. Note that the PUC has six DOFs (five bar elements) and that the periodic boundary condition relates u_1 to u_6, resulting in five independent DOFs for the global displacement vector $\boldsymbol{U}$. By considering the five elements of the PUC and by providing BFPBC (as shown in Eq. (3)), the system of equations $\boldsymbol{SU} = \boldsymbol{0}$ is:

$$\begin{bmatrix} 2a_1 & b_1 & 0 & 0 & e^{\mathrm{i}qL}b_1 \\ b_1 & a_{12} & b_2 & 0 & 0 \\ 0 & b_2 & a_{23} & b_3 & 0 \\ 0 & 0 & b_3 & a_{32} & b_2 \\ e^{-\mathrm{i}qL}b_1 & 0 & 0 & b_2 & a_{21} \end{bmatrix}\begin{bmatrix} u_1 \\ u_2 \\ u_3 \\ u_4 \\ u_5 \end{bmatrix} = \boldsymbol{0}, \tag{14}$$

where $a_{jk} = a_j + a_k$, while u_j is the DOF (displacement) associated to the jth node. The determinant of the coefficient matrix of Eq. (14) provides us with the characteristic equation relating the Bloch wave vector q with the applied frequency ω. The solution of this equation then yields the dispersion relation.

Noteworthy, the analytical solution of the determinant equation given by Eq. (14) only exists for simple cases as the one studied here. In most cases, however, such an analytical approach is not feasible, and the solution is found numerically [65]. The band structure is then obtained either by using a Newton–Raphson approach or another nonlinear solution procedure or by converting the system to a generalized eigenvalue problem by means of static condensation [65].

Similarly, by assembling DSMs to form the finite LRMM waveguide and by providing Dirichlet BC (as shown in Eq. (4)), we obtain the system of linear equations for **BVP 2**:

$$\boldsymbol{SU} = \boldsymbol{0}, \qquad \boldsymbol{S} = \mathop{\mathbb{A}}_{j\in\mathcal{J}_\Xi}\boldsymbol{s}_j. \tag{15}$$

The solution of Eq. (15) yields the displacement vector that is used to obtain displacement transmissibility.

2.1.1. *Throw-off element for reflection-free analysis*

To obtain displacement transmissibility without the effects of reflections from the free end, we model the waveguide with a non-reflective boundary. This can easily be attained using a special throw-off spectral element [64]. In contrast to standard spectral elements, where nodes are separated by a finite distance, in a throw-off element, one of the nodes is located at infinity. This element, therefore, draws energy out of the system continuously, resulting in a non-reflective boundary. The contribution to the dynamic stiffness matrix of such a throw-off element is given by:

$$s_\infty(\omega) = \mathrm{i}\kappa_j E_j A_j. \tag{16}$$

Note that this contribution, which needs to be added to the mesh node to which the throw-off element is connected, is always complex, and therefore the global stiffness matrix is also complex after assembly. This implies that the system always experiences dissipation in the presence of a throw-off element. In addition, $E_j A_j$ in Eq. (16) is directly related to the dissipation rate, *i.e.*, the higher its value, the greater the dissipation due to the throw-off element.

2.2. *FEM analysis*

The finite-dimensional counterpart of the variational form Eq. (5) is solved by means of standard FEM to compare both accuracy and computational costs. Contrary to SEM, where a single spectral element per subdomain is used to obtain the dynamic behavior, in FEM, such an approach leads to very poor accuracy—particularly at high frequencies. Instead, a PUC Π_i (or the entire domain Ξ in the case of the waveguide) is subdivided into a set of interconnected finite elements e_j to improve accuracy such that $\overline{\Pi}_i^h = \cup_{j\in\mathcal{E}}\overline{e}_j$ (or $\overline{\Xi}^h = \cup_{j\in\mathcal{E}}\overline{e}_j$), where $\mathcal{E}$ refers to the finite elements' index set, *e.g.*, for a uniform mesh size h, $\mathcal{E}_\Pi = \{1,\ldots,5/h\}$

(and $\mathcal{E}_{\Xi} = \{1, \ldots, 25/h\}$). The domain discretization $\overline{\Pi}_i^h$ (or $\overline{\Xi}^h$) is then associated with finite element function sets $\mathcal{U}^h, \mathcal{V}^h$ that are spanned by linear Lagrange shape functions, such that the trial solution $u^h \in \mathcal{U}^h$ and the weight function $w^h \in \mathcal{V}^h$ read:

$$\begin{aligned} u^h(x) &= \sum_{k \in \mathcal{K}} \varphi_k(x) U_k = \boldsymbol{\Phi} \boldsymbol{U}, \\ w^h(x) &= \sum_{k \in \mathcal{K}} \varphi_k(x) W_k = \boldsymbol{\Phi} \boldsymbol{W}, \end{aligned} \tag{17}$$

where $\mathcal{K}$ is the FE nodes' index set (that contains one additional index with respect to $\mathcal{E}$), and φ_k refers to the linear Lagrange shape function associated with ith DOF.

The finite-dimensional form of Eq. (5) then reads:

$$\sum_{j \in \mathcal{E}} \left[\int_{e_j} E_j A_j \frac{\partial u^h}{\partial x} \frac{\partial w^h}{\partial x} \, \mathrm{d}x + \int_{e_j} \rho_j A_j \frac{\partial^2 u^h}{\partial t^2} w^h \, \mathrm{d}x + \int_{e_j} \eta_j \frac{\partial u^h}{\partial t} w^h \, \mathrm{d}x \right] = 0 \quad \forall \, w^h \in \mathcal{V}^h. \tag{18}$$

By using Eq. (17) in Eq. (18), and noting that the statement $\forall \, w^h \in \mathcal{V}^h$ translates to $\forall \, \boldsymbol{W} \in \mathbb{R}^{|\mathcal{K}|}$ (since Lagrange shape functions are known), we arrive at our discrete system:

$$\left(\boldsymbol{K} - \omega^2 \boldsymbol{M} \right) \boldsymbol{U} = \boldsymbol{0}, \tag{19}$$

where as usual, the global stiffness matrix $\boldsymbol{K}$ and the global mass matrix $\boldsymbol{M}$ are obtained by assembling the contribution of local arrays:

$$\boldsymbol{K} = \mathop{\mathbb{A}}_{j \in \mathcal{E}} \boldsymbol{k}_j, \qquad \boldsymbol{M} = \mathop{\mathbb{A}}_{j \in \mathcal{E}} \boldsymbol{m}_j, \tag{20}$$

$$\boldsymbol{k}_j = \frac{E_j A_j}{h_j} \begin{bmatrix} 1 & -1 \\ -1 & 1 \end{bmatrix}, \quad \boldsymbol{m}_j = \rho_j A_j h_j \begin{bmatrix} 1/3 & 1/6 \\ 1/6 & 1/3 \end{bmatrix}. \tag{21}$$

In Eq. (21) h_j refers to the element size, which is not necessarily uniform throughout the FE discretization.

(19) can be used to describe both PUC and waveguide, as shown in Fig. 1. After providing BFPBC to the PUC (as per Eq. (3)) or Dirichlet BC to the waveguide (as per Eq. (4)), we obtain either the band structure or the displacement transmissibility, respectively.

2.3. Lumped-mass model of LRMM

In the lumped-mass model (LMM), all elements of the PUC are represented as point masses interconnected by springs. In this model, we retain the stiffnesses of the subsections of the PUC, whereas masses are lumped to the nodes connecting the springs. Therefore, the PUC's LMM has only five DOFs. The expressions and values for masses m_1 through m_5 and stiffnesses k_1 through k_4 are given in Table 2. Noteworthy, the stiffness of the lead block is not considered because, for practical purposes, it acts as a rigid body.

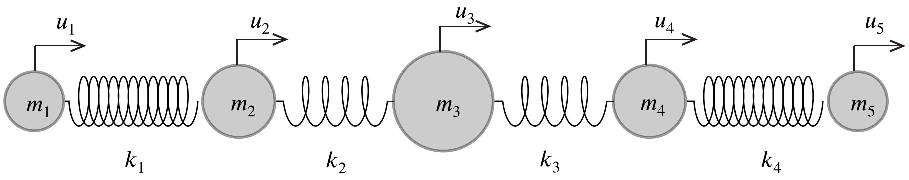

Fig. 2. Schematic of the PUC's LMM, showing the subsections as masses m_1 through m_5 interconnected by springs k_1 through k_4. u_1 through u_5 are the displacements of the corresponding point masses. Here the periodicity is between m_1 and m_5.

Table 2
Expressions and values of the parameters of LMM.

Mass (kg)	Stiffness (N/m)
$m_1 = \frac{\rho_1 A_1 l_1}{2} = 3.44 \times 10^{-4}$	$k_1 = \frac{E_1 A_1}{l_1} = 56250$
$m_2 = \frac{\rho_1 A_1 l_1}{2} + \frac{\rho_2 A_2 l_2}{2} = 3.85 \times 10^{-4}$	$k_2 = \frac{E_2 A_2}{l_2} = 139.19$
$m_3 = \rho_2 A_2 l_2 + \rho_3 A_3 l_3 = 1.25 \times 10^{-2}$	$k_3 = \frac{E_2 A_2}{l_2} = 139.19$

Also $m_4 = m_2$, $m_5 = m_1$, and $k_4 = k_1$.

The equations of motion for this LMM are obtained by balancing forces. Here we use superscripts to index the periodic unit cells and subindices to index the PUC's subdomains. Therefore, let $u_1^{(j)}$ through $u_5^{(j)}$ represent the displacements of masses m_1 through m_5 for the jth unit cell (Fig. 2). Since the periodicity is between $u_1^{(j)}$ and $u_5^{(j)}$, $m_1^{(j)}$ is connected to $m_5^{(j-1)}$. Correspondingly, $m_5^{(j)}$ is connected to the $m_1^{(j+1)}$. The force balance of each of the masses in the periodic unit cell is:

$$\begin{aligned}
m_1\ddot{u}_1^{(j)} + k_1\left(u_1^{(j)} - u_2^{(j)}\right) + k_4\left(u_1^{(j)} - u_5^{(j-1)}\right) &= 0,\\
m_2\ddot{u}_2^{(j)} + k_1\left(u_2^{(j)} - u_1^{(j)}\right) + k_2\left(u_2^{(j)} - u_3^{(j)}\right) &= 0,\\
m_3\ddot{u}_3^{(j)} + k_2\left(u_3^{(j)} - u_2^{(j)}\right) + k_3\left(u_3^{(j)} - u_4^{(j)}\right) &= 0,\\
m_4\ddot{u}_4^{(j)} + k_3\left(u_4^{(j)} - u_3^{(j)}\right) + k_4\left(u_4^{(j)} - u_5^{(j)}\right) &= 0,\\
m_5\ddot{u}_5^{(j)} + k_4\left(u_5^{(j)} - u_4^{(j)}\right) + k_1\left(u_5^{(j)} - u_1^{(j+1)}\right) &= 0.
\end{aligned} \tag{22}$$

Applying BFPBC to (22) and further processing provides us the matrix equation for the jth PUC:

$$\begin{bmatrix} d_{11} & -k_1 & 0 & 0 & -e^{\mathrm{i}qL}k_1 \\ -k_1 & d_{12} & -k_2 & 0 & 0 \\ 0 & -k_2 & d_{23} & -k_2 & 0 \\ 0 & 0 & -k_2 & d_{12} & -k_1 \\ -e^{-\mathrm{i}qL}k_1 & 0 & 0 & -k_1 & d_{11} \end{bmatrix} \begin{bmatrix} u_1^{(j)} \\ u_2^{(j)} \\ u_3^{(j)} \\ u_4^{(j)} \\ u_5^{(j)} \end{bmatrix} = \mathbf{0}, \tag{23}$$

where $d_{ij} = k_i + k_j - m_j\omega^2$. The non-trivial solution of this system is obtained by equating the determinant of the coefficient matrix of Eq. (23) to zero, and this result provides us with the dispersion relation.

2.4. Incorporating damping (viscous and viscoelastic) in SEM

The effects of the constant viscous damping have been incorporated in the dynamic stiffness matrix given by Eq. (12) via the damping factor η. However, this factor remains constant throughout the analysis, and therefore it does not capture the effects of frequency on damping. Because most of the damping behavior of polymers and elastomers has a high dependence on the applied frequency, we include frequency-dependent viscoelastic effects in our SEM model to obtain a more realistic behavior for the LRMM [73].

A straightforward means to account for viscoelasticity is using the Kelvin–Voigt model, a spring-dashpot system connected in parallel, as shown in Fig. 3(a). According to this model, the effective complex Young's modulus takes the form:

$$\hat{E}\left(\mathrm{i}\omega\right) = E + \mathrm{i}\omega\eta/A. \tag{24}$$

The spring element has its stiffness value equal to the real part E, also called storage modulus, whereas the frictional resistance of the dashpot accounts for the viscosity contribution η.

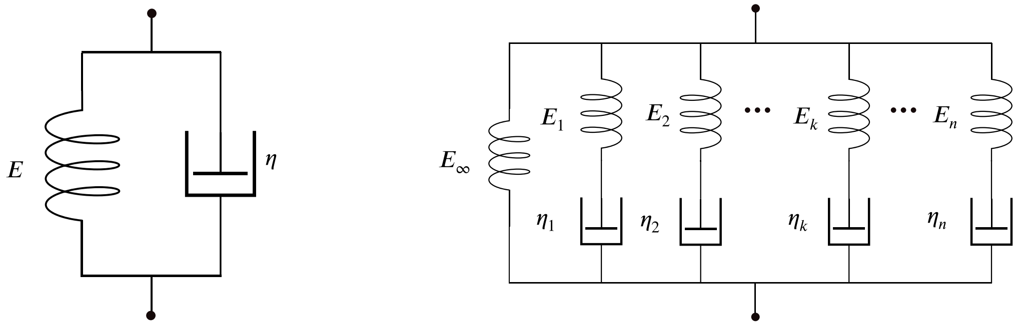

(a) (b)

Fig. 3. Linear viscoelastic models. (a) Kelvin–Voigt model; and (b) generalized Maxwell model. E_i and η_i, respectively, represent the stiffness of spring and resistance of dashpot of ith Maxwell element.

Because of its simplicity (*i.e.,* single spring and dashpot system), the Kelvin–Voigt model will not capture the exact viscoelastic behavior of the waveguide. Consequently, we also use the generalized Maxwell model (Fig. 3(b)), which uses a spring-dashpot (Maxwell element) chain connected in parallel. Each of these elements corresponds to a particular loading rate. The more the number of elements present in the model, the better the approximation towards the actual dynamic behavior of the system. The behavior of the individual elements is usually through experiments, for instance, by means of dynamic mechanical analysis [74]. The effective complex Young's modulus in this model is expressed as a series representation, known as the Prony series:

$$\hat{E}\left(\mathrm{i}\omega\right) = E_\infty + \sum_{i=1}^{n} \frac{\mathrm{i}\omega E_i}{\mathrm{i}\omega\tau_i + 1}, \tag{25}$$

where $\tau_i = \eta_i / E_i$ and E_i denote, respectively, the ith Maxwell element's relaxation time and corresponding relaxation modulus, and E_∞ is Young's modulus at equilibrium. The number n is usually chosen based on an adequate fit with experimental data. Table 3 shows the Prony series for teflon [75] and rubber [76].

Table 3
Relaxation times and relaxation moduli for teflon and rubber Prony series.

Teflon		Rubber	
τ_i (s)	E_i (Pa)	τ_i (s)	E_i (Pa)
0.1	444.86×10^6	4.32×10^{-9}	9×10^6
1	365.68×10^6	5.84×10^{-8}	4.2×10^6
10	298.73×10^6	3.51×10^{-7}	2.94×10^6
100	259.31×10^6	2.28×10^{-6}	2.41×10^6
1000	237.57×10^6	1.68×10^{-5}	1.87×10^6
		2.82×10^{-4}	1.31×10^6
		7.96×10^{-3}	7.02×10^5
		9.5×10^{-3}	4.45×10^5
∞	210.5×10^6	∞	4.12×10^5

3. Results and discussions

3.1. Dispersion relation comparison

We begin this section by comparing the undamped dispersion relations of our 1D LRMM using SEM, FEM, and LMM. As explained earlier, the dispersion relation is obtained by analyzing the periodic unit cell with prescribed Bloch–Floquet boundary conditions—which assumes an infinite material. The lengths and cross sectional areas of the subdomains in the periodic unit cell are shown in Table 4.

Table 4
Geometric properties for PUC's subdomains.

Material	Length (cm)	Cross sectional area (mm^2)
Teflon	5	6.25
Rubber	7.4	1
Lead	2	54.8

Fig. 4 shows the complex dispersion diagram; while the real part indicates various propagation modes and BGs (shown in shaded regions), the imaginary part represents the rate of attenuation in amplitude for its corresponding frequency in the BG. Since frequency is the independent parameter throughout SEM analysis, it is straightforward to obtain the imaginary part of the wave vector. Every propagation mode has zero imaginary part, *i.e.*, the imaginary wave vectors correspond to evanescent waves. The larger the value of the imaginary part of the wave vector, the higher the corresponding attenuation rate. The LMM results in Fig. 4 show three modes and their corresponding attenuation rates. However, only the first two modes – which define the first band gap – are predicted accurately; the three remaining modes (the 4th and 5th modes are not shown in Fig. 4) are not accurate due to LMM treating bars as point masses connected by linear springs. The results obtained by FEM are more accurate. Although FEM predicts all modes of the LRMM, the computational cost increases with increasing frequency. In the FEM results shown in Fig. 4, we used 50 elements for the first mode and 2500 elements for the fifth mode to keep up with the accuracy of SEM. For simplicity, we have kept the number of elements per section of the PUC constant, *i.e.*, every section shown in Fig. 1 will have elements of different lengths compared to the elements in the adjacent subsection. Also, in contrast to SEM and LMM, the independent parameter in our FEM analysis is the wave vector *i.e.*, $\omega(k)$ approach is used here; thus, it is difficult to obtain the imaginary part of the dispersion diagram via our FEM model (and it is thus not shown). Although by using the $k(\omega)$ approach, one can obtain the imaginary part via FEM, the analysis is more complicated due to coordinate inversion and static condensation [77]. SEM has the highest accuracy in predicting all modes and their attenuation rates. The frequency-dependent shape functions aid SEM in capturing the actual dynamic behavior with very little computational cost—five elements for the entire frequency spectrum! It is noteworthy that although the computational cost primarily depends on the total number of elements (or DOFs), the shape functions also influence it. Since SEM uses complex shape functions compared to linear polynomials used by FEM, the cost per evaluation of one element is higher for SEM compared to FEM. Nevertheless, this variation vanishes quickly, as FEM needs several elements to describe the dynamic response, which increases with frequency. However, SEM only requires one element, irrespective of the operating frequency. For instance, in the band structure analysis, the number of elements per section in FEM (for the highest frequency) was 500 times higher than the corresponding SEM model; the computational cost of the former is higher than the latter.

3.2. Undamped transmissibility comparison

In the previous section, we showed that SEM is highly accurate and computationally inexpensive. Because the band structure analysis assumes an infinite number of PUCs, the dispersion relation may not faithfully represent the dynamic behavior of a waveguide composed of a finite number of unit cells. We characterize the finite waveguide using displacement transmissibility,

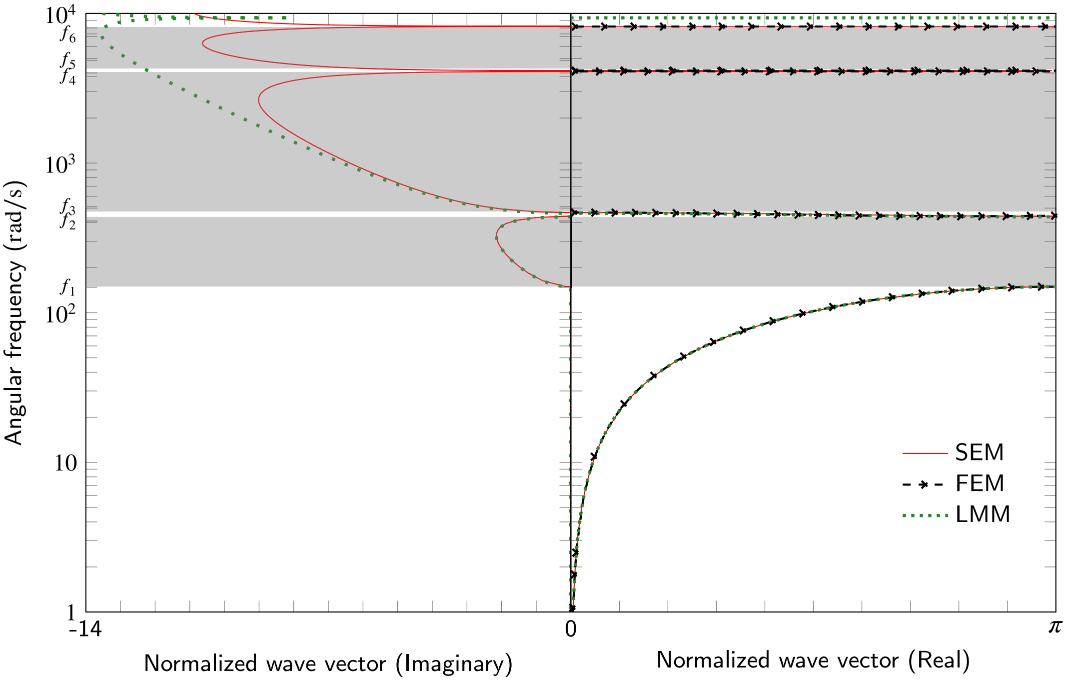

Fig. 4. Frequency as a function of non-dimensional complex wave vector (dispersion relation) for our 1D LRMM using SEM, FEM, and LMM, where the shaded regions represent BGs. The BG bounding frequencies are $f_1 = 148\,\text{radian/s}$, $f_2 = 441\,\text{radian/s}$, $f_3 = 470\,\text{radian/s}$, $f_4 = 4100\,\text{radian/s}$, $f_5 = 4250\,\text{radian/s}$, $f_6 = 8200\,\text{radian/s}$. SEM predicts the band structure, including attenuation rates exactly, whereas FEM can only predict results accurately with very high computational cost (particularly at high frequencies). LMM yields good results only for the modes that define the first BG.

whereby the steady-state response of the waveguide is obtained, and the ratio between output displacement (at the right end of the waveguide) to the prescribed input displacement (at the other end) is acquired. This is done for a given applied harmonic frequency, and thus frequency sweep analysis is done to get the behavior for a large range of frequencies.

Fig. 5 illustrates the undamped displacement transmissibility for FEM and SEM (with and without a throw-off element). Both FEM and SEM capture BGs predicted by the dispersion relation accurately (as shown in shaded regions). To simplify FEM analysis, the number of elements has been kept constant (500 per subsection). As expected, the transmissibility results of FEM are more accurate at low frequencies since the number of elements per wavelength is fixed and the wavelength is larger for smaller frequencies, enabling more elements at those frequencies.

The peaks in the transmission before the band gaps result from sub-system resonances, which are resonant modes present in the finite waveguide and are due to multiple reflections from the free end that are not accounted for in the band structure analysis. Both FEM and SEM capture these peaks effectively.

The displacement transmissibility of SEM with the throw-off element shows considerable differences in the amplitudes outside the BGs since all peaks due to reflections are absent. For frequencies with higher attenuation (after the first BG) where fewer reflections are present, the response of both SEM models is close.

3.3. Effects of damping

In this section, we compare the transmissibility between undamped and damped LRMMs with the throw-off element using various damping models. The results are given in Fig. 6, which shows that constant viscous damping reduces the transmission further and that this effect is more pronounced at low frequencies. Even though the resonant peaks are also reduced at higher frequencies, viscous damping does not show any prominent effects on the rest of the transmission spectra.

As discussed in Section 2.4, viscoelastic models are essential to describe the proper dynamic behavior of LRMM waveguides comprised of polymers and elastomers. The figure also shows the transmissibility considering Kelvin–Voigt viscoelastic and generalized Maxwell viscoelastic damped SEM models. Although the Kelvin–Voigt model (Fig. 3(a)) is straightforward to implement, the use of a single spring and dashpot does not provide very realistic dynamic behavior. As shown in Fig. 6, this simple damping model behaves close to purely viscous at low frequencies and slowly transitions to purely elastic at high frequencies. The generalized Maxwell damping model predicts the viscoelastic behavior more accurately due to the presence of multiple Maxwell elements. As apparent from the figure, this model influences the entire frequency spectrum. It is worth noting that with this model, the first BG (due to Mie scattering) shifts down in frequency range. Additionally, in the generalized Maxwell model, there is less separation between attenuating and propagating regions (of frequencies) because due to the dissipation, there is always attenuation present

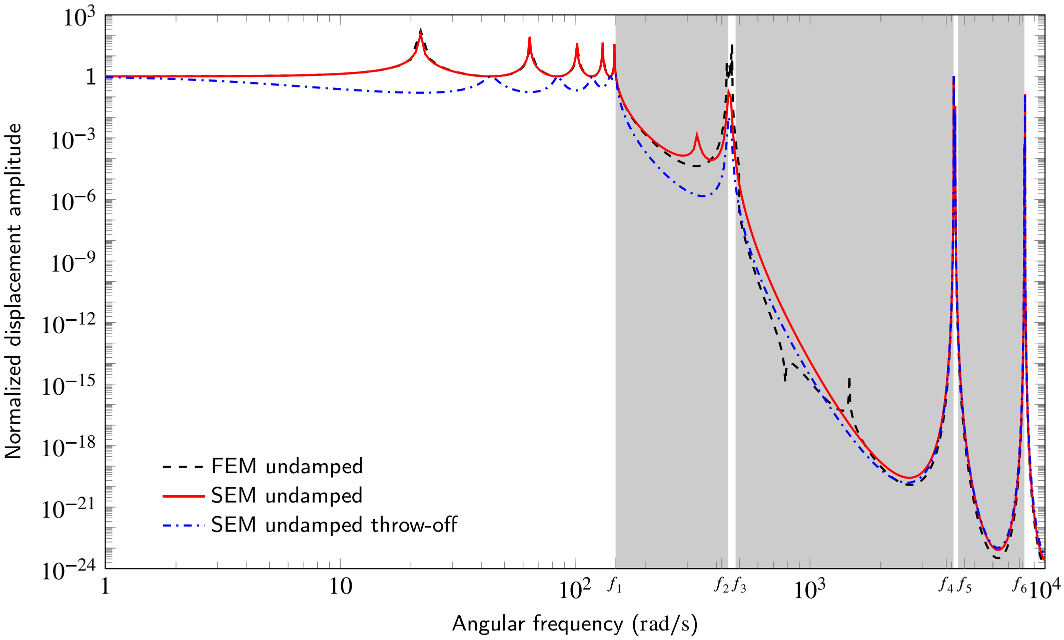

Fig. 5. Displacement transmissibility for an undamped five PUC LRMM waveguide using FEM and SEM (with and without a throw-off element). The curves capture the BGs predicted by the dispersion relation, as shown in the shaded region marked by frequencies f_1 through f_6. The displacements match at initial frequency ranges but start to diverge at higher frequencies due to the lack of an adequate number of elements in the FE model. Due to the non-reflective BC, all the peaks in displacement due to reflections are absent in SEM with a throw-off element. It can also be noted that within the BGs, where fewer reflections are present, the SEM curves with and without the throw-off element are close.

in the system. As explained previously, the accuracy of this model depends greatly on the number of elements in the Prony series, which in our case is five for teflon and eight for rubber. Increasing the number of terms in the Prony series, which is beyond the scope of this study, could further improve the results.

4. Conclusions

In this manuscript, we investigated 1D undamped and damped LRMMs using lumped-mass, finite element, and spectral element models. The dispersion relation revealed that the accuracy of the lumped-mass model was limited only to the two modes that define the band gap due to Mie scattering; higher modes have a very poor agreement with the true dynamic behavior of the MM. The finite element distributed-mass model showed good agreement with SEM in the dispersion relation. However, to obtain a matching response, the total DOFs of FEM increased rapidly for high frequencies. In addition, with little effort, SEM could provide the imaginary part of the dispersion relation, which indicates the amplitude attenuation rates within BGs. This is very beneficial in designing a finite LRMM waveguide targeted to reduce a given amplitude for a specific frequency range. Indeed, the imaginary part gives an estimation of the amplitude attenuation rate for a given frequency and a number of units, and this can be used for a first back-of-envelope calculation.

We showed that extending the spectral element model to analyze a finite LRMM waveguide composed of five unit cells was also straightforward. Because many applications require a reflection-free response, we extended the model to incorporate a non-reflective boundary using a throw-off element, which allows to conduit energy out of the system.

Incorporating viscous and viscoelastic damping effects into SEM models proved to be straightforward as well. Even though constant viscous damping shows a reduction in transmission, it does not capture the response accurately throughout the frequency spectrum as most of the components of this LRMM are visco-elastic. Due to its simplicity, the Kelvin–Voigt model was also unable to accurately predict the LRMM waveguide's dynamic response. The generalized Maxwell model provided the most accurate response for the entire frequency range and revealed a shift in the first BG to lower frequencies. Because the accuracy of the generalized Maxwell model is tightly coupled to its Prony series, further research is needed to investigate the use of this model in LRMMs.

We conclude that SEM is the preferred methodology for analyzing the damped/undamped dynamic response of one-dimensional LRMMs regardless of the frequency. Besides, SEM directly provides the complete band structure (both real and imaginary), which includes various modes, BGs, and corresponding attenuation rates compared with other distributed-mass methods, such as FEM, where finding the imaginary part is cumbersome. Although SEM cannot be used to model complex geometries, it can still be used as a rough approximation or for a back-of-the-envelope preliminary LRMM design. A future direction could be to perform transmission experiments using viscoelastic phononic crystals to validate the predictions from the numerical/analytical methods discussed here.

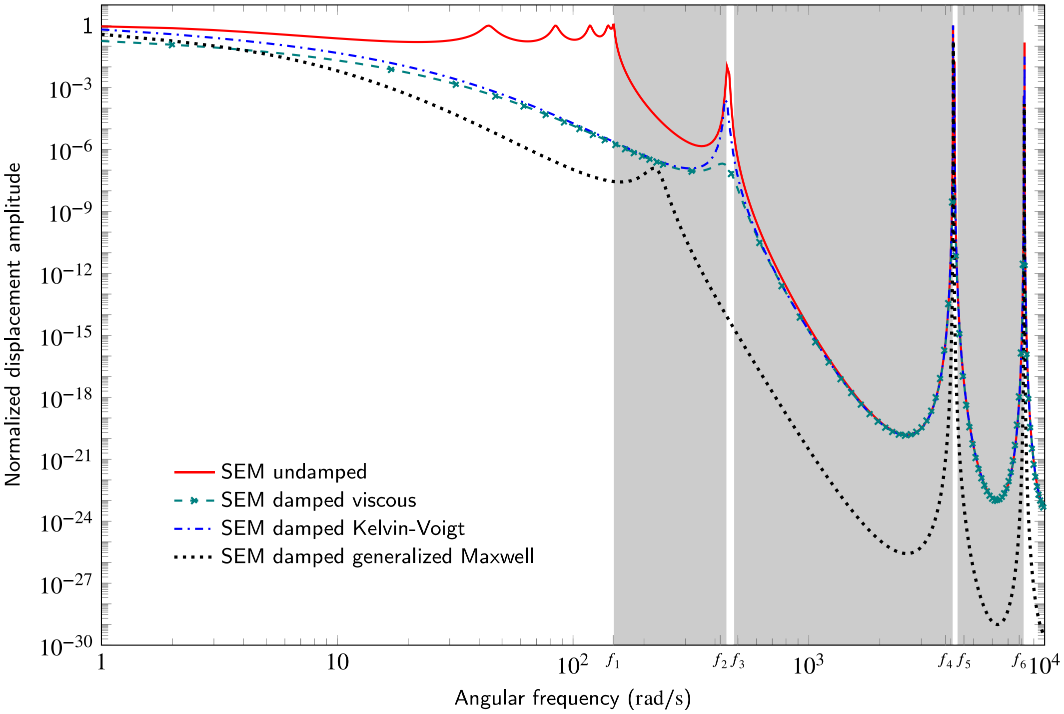

Fig. 6. Transmissibility relation between undamped, viscous damped, and viscoelastic damped models where the BGs are shaded with their bounds marked in the abscissa. Viscous damping affects mostly lower frequency ranges and resonant peaks because it does not account for frequency variation. The Kelvin–Voigt viscoelastic model transitions from viscous to elastic with increasing frequency. The damped dynamic behavior is further improved by means of the generalized Maxwell model, which affects the entire frequency spectrum and shifts the first BG to lower frequencies. Yet, the latter's accuracy depends on the number of elements in the Prony series.

CRediT authorship contribution statement

Sabiju Valiya Valappil: Writing – original draft, Software, Resources, Methodology, Investigation, Formal analysis, Data curation, Conceptualization. **Alejandro M. Aragón:** Writing – review & editing, Supervision, Funding acquisition, Conceptualization.

Declaration of competing interest

The authors declare that they have no known competing financial interests or personal relationships that could have appeared to influence the work reported in this paper.

Acknowledgments

The authors greatly appreciate the financial support from the topconsortium voor kennis en innovatie (TKI) grant and our funding partner KROHNE.

Data availability

Data will be made available on request.

References

[1] M.S. Kushwaha, P. Halevi, L. Dobrzynski, B. Djafari-Rouhani, Acoustic band structure of periodic elastic composites, Phys. Rev. Lett. 71 (1993) 2022–2025.

[2] Steven A. Cummer, Johan Christensen, Andrea Alù, Controlling sound with acoustic metamaterials, Nat. Rev. Mater. 1 (3) (2016) 16001.

[3] Matthew Reynolds, Stephen Daley, An active viscoelastic metamaterial for isolation applications, Smart Mater. Struct. 23 (4) (2014) 045030.

[4] A.A. Maznev, A.G. Every, O.B. Wright, Reciprocity in reflection and transmission: What is a 'phonon diode'? Wave Motion 50 (4) (2013) 776–784.

[5] Osama R. Bilal, André Foehr, Chiara Daraio, Bistable metamaterial for switching and cascading elastic vibrations, Proc. Natl. Acad. Sci. 114 (18) (2017) 4603–4606.

[6] Kyung Ho Sun, Jae Eun Kim, Jedo Kim, Kyungjun Song, Sound energy harvesting using a doubly coiled-up acoustic metamaterial cavity, Smart Mater. Struct. 26 (7) (2017) 075011.

[7] Shu Zhang, Leilei Yin, Nicholas Fang, Focusing ultrasound with an acoustic metamaterial network, Phys. Rev. Lett. 102 (19) (2009) 194301.

[8] Choon Mahn Park, Jong Jin Park, Seung Hwan Lee, Yong Mun Seo, Chul Koo Kim, Sam H. Lee, Amplification of acoustic evanescent waves using metamaterial slabs, Phys. Rev. Lett. 107 (2011) 194301.

[9] Chengrong Ma, Shuxiang Gao, Ying Cheng, Xiaojun Liu, Acoustic metamaterial antennas for combined highly directive-sensitive detection, Appl. Phys. Lett. 115 (5) (2019) 053501.

[10] J. Xu, J. Tang, Tunable prism based on piezoelectric metamaterial for acoustic beam steering, Appl. Phys. Lett. 110 (18) (2017) 181902.

[11] Hyuk Lee, Jun Kyu Lee, Hong Min Seung, Yoon Young Kim, Mass-stiffness substructuring of an elastic metasurface for full transmission beam steering, J. Mech. Phys. Solids 112 (2018) 577–593.

[12] Shu Zhang, Chunguang Xia, Nicholas Fang, Broadband acoustic cloak for ultrasound waves, Phys. Rev. Lett. 106 (2) (2011) 024301.

[13] Mohamed Farhat, Sebastien Guenneau, Stefan Enoch, Ultrabroadband elastic cloaking in thin plates, Phys. Rev. Lett. 103 (2) (2009) 024301.

[14] Nicolas Stenger, Manfred Wilhelm, Martin Wegener, Experiments on elastic cloaking in thin plates, Phys. Rev. Lett. 108 (1) (2012) 014301.

[15] H.K. Zhang, Yi Chen, X.N. Liu, G.K. Hu, An asymmetric elastic metamaterial model for elastic wave cloaking, J. Mech. Phys. Solids 135 (2020) 103796.

[16] Yong Li, Bin Liang, Zhong-ming Gu, Xin-ye Zou, Jian-chun Cheng, Reflected wavefront manipulation based on ultrathin planar acoustic metasurfaces, Sci. Rep. 3 (2013) 2546.

[17] Fabrice Lemoult, Mathias Fink, Geoffroy Lerosey, Acoustic resonators for far-field control of sound on a subwavelength scale, Phys. Rev. Lett. 107 (6) (2011) 064301.

[18] H.H. Huang, C.T. Sun, G.L. Huang, On the negative effective mass density in acoustic metamaterials, Internat. J. Engrg. Sci. 47 (4) (2009) 610–617.

[19] Sébastien Guenneau, Alexander Movchan, Gunnar Pétursson, S. Anantha Ramakrishna, Acoustic metamaterials for sound focusing and confinement, New J. Phys. 9 (11) (2007) 399.

[20] Yong Xiao, Jihong Wen, Xisen Wen, Longitudinal wave band gaps in metamaterial-based elastic rods containing multi-degree-of-freedom resonators, New J. Phys. 14 (3) (2012) 033042.

[21] H.H. Huang, C.T. Sun, Wave attenuation mechanism in an acoustic metamaterial with negative effective mass density, New J. Phys. 11 (1) (2009) 013003.

[22] H.H. Huang, C.T. Sun, Locally resonant acoustic metamaterials with 2D anisotropic effective mass density, Phil. Mag. 91 (6) (2011) 981–996.

[23] Hsin-Haou Huang, Chin-Teh Sun, Anomalous wave propagation in a one-dimensional acoustic metamaterial having simultaneously negative mass density and Young's modulus, J. Acoust. Soc. Am. 132 (4) (2012) 2887–2895.

[24] H.H. Huang, C.T. Sun, Theoretical investigation of the behavior of an acoustic metamaterial with extreme Young's modulus, J. Mech. Phys. Solids 59 (10) (2011) 2070–2081.

[25] Raj K. Narisetti, Michael J. Leamy, Massimo Ruzzene, A perturbation approach for predicting wave propagation in one-dimensional nonlinear periodic structures, J. Vib. Acoust. 132 (3) (2010) 031001.

[26] Raj K. Narisetti, Massimo Ruzzene, Michael J. Leamy, Study of wave propagation in strongly nonlinear periodic lattices using a harmonic balance approach, Wave Motion 49 (2) (2012) 394–410.

[27] Romik Khajehtourian, Mahmoud I. Hussein, Dispersion characteristics of a nonlinear elastic metamaterial, AIP Adv. 4 (12) (2014) 124308.

[28] Myung Hwan Bae, Joo Hwan Oh, Amplitude-induced bandgap: New type of bandgap for nonlinear elastic metamaterials, J. Mech. Phys. Solids (2020) 103930.

[29] Mahmoud I. Hussein, Michael J. Frazier, Band structure of phononic crystals with general damping, J. Appl. Phys. 108 (9) (2010) 093506.

[30] Mahmoud I. Hussein, Michael J. Frazier, Metadamping: An emergent phenomenon in dissipative metamaterials, J. Sound Vib. 332 (20) (2013) 4767–4774.

[31] Michael J. Frazier, Mahmoud I. Hussein, Viscous-to-viscoelastic transition in phononic crystal and metamaterial band structures, J. Acoust. Soc. Am. 138 (5) (2015) 3169–3180.

[32] Michael J. Frazier, Mahmoud I. Hussein, Generalized Bloch's theorem for viscous metamaterials: Dispersion and effective properties based on frequencies and wavenumbers that are simultaneously complex, Comptes Rendus Phys. 17 (5) (2016) 565–577.

[33] G.L. Huang, C.T. Sun, Band gaps in a multiresonator acoustic metamaterial, J. Vib. Acoust. 132 (3) (2010) 031003.

[34] P. Frank Pai, Metamaterial-based broadband elastic wave absorber, J. Intell. Mater. Syst. Struct. 21 (5) (2010) 517–528.

[35] Yongquan Liu, Xianyue Su, C.T. Sun, Broadband elastic metamaterial with single negativity by mimicking lattice systems, J. Mech. Phys. Solids 74 (2015) 158–174.

[36] Hongfei Zhu, Sansit Patnaik, Timothy F. Walsh, Bradley H. Jared, Fabio Semperlotti, Nonlocal elastic metasurfaces: Enabling broadband wave control via intentional nonlocality, Proc. Natl. Acad. Sci. 117 (42) (2020) 26099–26108.

[37] Y.Y. Chen, G.L. Huang, C.T. Sun, Band gap control in an active elastic metamaterial with negative capacitance piezoelectric shunting, J. Vib. Acoust. 136 (6) (2014).

[38] Kwek Tze Tan, H.H. Huang, C.T. Sun, Blast-wave impact mitigation using negative effective mass density concept of elastic metamaterials, Int. J. Impact Eng. 64 (2014) 20–29.

[39] Yukihiro Tanaka, Shin-ichiro Tamura, Surface acoustic waves in two-dimensional periodic elastic structures, Phys. Rev. B 58 (12) (1998) 7958.

[40] Zhilin Hou, Badreddine M. Assouar, Modeling of Lamb wave propagation in plate with two-dimensional phononic crystal layer coated on uniform substrate using plane-wave-expansion method, Phys. Lett. A 372 (12) (2008) 2091–2097.

[41] C. Charles, Bernard Bonello, François Ganot, Propagation of guided elastic waves in 2D phononic crystals, Ultrasonics 44 (2006) e1209–e1213.

[42] Yongjun Cao, Zhilin Hou, Youyan Liu, Convergence problem of plane-wave expansion method for phononic crystals, Phys. Lett. A 327 (2–3) (2004) 247–253.

[43] C. Cetinkaya, Alexander F. Vakakis, Transient axisymmetric stress wave propagation in weakly coupled layered structures, J. Sound Vib. 194 (3) (1996) 389–416.

[44] H. Al Ba'ba'a, M. Nouh, An investigation of vibrational power flow in one-dimensional dissipative phononic structures, J. Vib. Acoust. 139 (2) (2017) 021003.

[45] Jose Miguel Luque-Raigon, Janne Halme, Hernan Miguez, Gabriel Lozano, Symmetry analysis of the numerical instabilities in the transfer matrix method, J. Opt. 15 (12) (2013) 125719.

[46] V. Cutanda Henríquez, P. Risby Andersen, J Søndergaard Jensen, P. Møller Juhl, Jose Sánchez-Dehesa, A numerical model of an acoustic metamaterial using the boundary element method including viscous and thermal losses, J. Comput. Acoust. 25 (04) (2017) 1750006.

[47] Muhammad Mushtaq, Nawazish Ali Shah, Ghulam Muhammad, Advantages and disadvantages of boundary element methods for compressible fluid flow problems, J. Am. Sci. 6 (1) (2010) 162–165.

[48] X.N. Liu, G.K. Hu, C.T. Sun, G.L. Huang, Wave propagation characterization and design of two-dimensional elastic chiral metacomposite, J. Sound Vib. 330 (11) (2011) 2536–2553.

[49] Ying Liu, Ling-tian Gao, Explicit dynamic finite element method for band-structure calculations of 2D phononic crystals, Solid State Commun. 144 (3–4) (2007) 89–93.

[50] Kathryn H. Matlack, Anton Bauhofer, Sebastian Krödel, Antonio Palermo, Chiara Daraio, Composite 3D-printed metastructures for low-frequency and broadband vibration absorption, Proc. Natl. Acad. Sci. 113 (30) (2016) 8386–8390.

[51] Hao-Wen Dong, Sheng-Dong Zhao, Yue-Sheng Wang, Chuanzeng Zhang, Topology optimization of anisotropic broadband double-negative elastic metamaterials, J. Mech. Phys. Solids 105 (2017) 54–80.

[52] Anastasiia O. Krushynska, Varvara G. Kouznetsova, Marc G.D. Geers, Towards optimal design of locally resonant acoustic metamaterials, J. Mech. Phys. Solids 71 (2014) 179–196.

[53] P. Frank Pai, Hao Peng, Shuyi Jiang, Acoustic metamaterial beams based on multi-frequency vibration absorbers, Int. J. Mech. Sci. 79 (2014) 195–205.

[54] E.D. Nobrega, F. Gautier, A. Pelat, JMC Dos Santos, Vibration band gaps for elastic metamaterial rods using wave finite element method, Mech. Syst. Signal Process. 79 (2016) 192–202.

[55] Romik Khajehtourian, Dennis M. Kochmann, A continuum description of substrate-free dissipative reconfigurable metamaterials, J. Mech. Phys. Solids (2020) 104217.

[56] A.O. Krushynska, V.G. Kouznetsova, M.G.D. Geers, Visco-elastic effects on wave dispersion in three-phase acoustic metamaterials, J. Mech. Phys. Solids 96 (2016) 29–47.

[57] M.A. Lewińska, V.G. Kouznetsova, J.A.W. van Dommelen, A.O. Krushynska, M.G.D. Geers, The attenuation performance of locally resonant acoustic metamaterials based on generalised viscoelastic modelling, Int. J. Solids Struct. 126 (2017) 163–174.

[58] Yan-Feng Wang, Yue-Sheng Wang, Vincent Laude, Wave propagation in two-dimensional viscoelastic metamaterials, Phys. Rev. B 92 (10) (2015) 104110.

[59] Joseph L. Rose, A baseline and vision of ultrasonic guided wave inspection potential, J. Press. Vessel. Technol. 124 (3) (2002) 273–282.

[60] Linlin Shi, Yuanguo Zhou, Jia-Min Wang, Mingwei Zhuang, Na Liu, Qing Huo Liu, Spectral element method for elastic and acoustic waves in frequency domain, J. Comput. Phys. 327 (2016) 19–38.

[61] Linlin Shi, Na Liu, Jianyang Zhou, Yuanguo Zhou, Jiamin Wang, Qing Huo Liu, Spectral element method for band-structure calculations of 3D phononic crystals, J. Phys. D: Appl. Phys. 49 (45) (2016) 455102.

[62] Anthony T. Patera, A spectral element method for fluid dynamics: Laminar flow in a channel expansion, J. Comput. Phys. 54 (3) (1984) 468–488.

[63] Dimitri Komatitsch, Jean-Pierre Vilotte, The spectral element method: An efficient tool to simulate the seismic response of 2D and 3D geological structures, Bull. Seismol. Soc. Am. 88 (2) (1998) 368–392.

[64] James F. Doyle, Wave propagation in structures, in: Wave Propagation in Structures, Springer, 1989, pp. 126–156.

[65] Usik Lee, Spectral Element Method in Structural Dynamics, John Wiley & Sons, 2009.

[66] Yong Xiao, Jihong Wen, Gang Wang, Xisen Wen, Theoretical and experimental study of locally resonant and Bragg band gaps in flexural beams carrying periodic arrays of beam-like resonators, J. Vib. Acoust. 135 (4) (2013).

[67] Filippo Casadei, Katia Bertoldi, Wave propagation in beams with periodic arrays of airfoil-shaped resonating units, J. Sound Vib. 333 (24) (2014) 6532–6547.

[68] Zhi-Jing Wu, Feng-Ming Li, Chuanzeng Zhang, Vibration band-gap properties of three-dimensional kagome lattices using the spectral element method, J. Sound Vib. 341 (2015) 162–173.

[69] Zhijing Wu, Fengming Li, Chuanzeng Zhang, Band-gap analysis of a novel lattice with a hierarchical periodicity using the spectral element method, J. Sound Vib. 421 (2018) 246–260.

[70] J.-H. Song, S.-Y. Hong, Vibration analysis of beams treated with passive constrained layer damping using spectral element method, J. Acoust. Soc. Am. 118 (3) (2005) 1865.

[71] Felix Bloch, Über die quantenmechanik der elektronen in kristallgittern, Z. Phys. 52 (7–8) (1929) 555–600.

[72] Thomas J.R. Hughes, The Finite Element Method: Linear Static and Dynamic Finite Element Analysis, Courier Corporation, 2012.

[73] Richard Christensen, Theory of Viscoelasticity: An Introduction, Elsevier, 2012.

[74] David S. Jones, Dynamic mechanical analysis of polymeric systems of pharmaceutical and biomedical significance, Int. J. Pharm. 179 (2) (1999) 167–178.

[75] Felicia Stan, Catalin Fetecau, Study of stress relaxation in polytetrafluoroethylene composites by cylindrical macroindentation, Compos. Part B: Eng. 47 (2013) 298–307.

[76] B. Merheb, P.A. Deymier, M. Jain, M. Aloshyna-Lesuffleur, S. Mohanty, A. Berker, R.W. Greger, Elastic and viscoelastic effects in rubber/air acoustic band gap structures: A theoretical and experimental study, J. Appl. Phys. 104 (6) (2008) 064913.

[77] Istvan A. Veres, Thomas Berer, Osamu Matsuda, Complex band structures of two dimensional phononic crystals: Analysis by the finite element method, J. Appl. Phys. 114 (8) (2013) 083519.